International Journal of Thermal Sciences 49 (2010) 653–663

Contents lists available at ScienceDirect

International Journal of Thermal Sciences

journal homepage: www.elsevier.com/locate/ijts

Numerical prediction of turbulent flow and heat transfer in helically coiled pipes

Ivan Di Piazza, Michele Ciofalo*

Dipartimento di Ingegneria Nucleare, Università degli Studi di Palermo, Viale delle Scienze, I-90128 Palermo, Italy

ARTICLE INFO

Article history:
Received 11 August 2009
Received in revised form
1 October 2009
Accepted 1 October 2009
Available online 30 October 2009

Keywords:
Helically coiled pipes
Curved pipes
Pressure drop
Heat transfer
Turbulent flow
Turbulence models

ABSTRACT

Computational results were obtained for turbulent flow and heat transfer in curved pipes, representative of helically coiled heat exchangers. Following a grid refinement study, grid independent predictions from alternative turbulence models (k–ε, SST k–ω and RSM–ω) were compared with DNS results and experimental pressure drop and heat transfer data. Using the SST k–ω and RSM–ω models, pressure drop results were in excellent agreement with literature data and the Ito correlation. For heat transfer, the literature is not comparably complete or accurate, but a satisfactory agreement was obtained in the range of available data. Unsatisfactory results, both for pressure drop and heat transfer, were given by the k–ε model with wall functions. Following the validation study, the RSM–ω model was used to compute friction coefficients and Nusselt numbers in the range Re = $1.4\cdot10^4$–$8\cdot10^4$, Pr = 0.7–5.6 and δ (coil curvature) = $3\cdot10^{-3}$–0.3. Power-law correlations were found unsuitable to fit the Re-, Pr- and δ-dependence of the Nusselt number, while the use of a properly formulated momentum-heat transfer analogy collapsed all results with high accuracy.

1. Introduction: flow and heat transfer in curved pipes and coils

Although curved pipes are used in a wide range of applications, flow in curved pipes is relatively less well known than that in straight ducts. Following the pioneering studies of Boussinesq [1] and Thomson [2] in the 19th century, Grindley and Gibson [3] noticed the effect of curvature on the fluid flow during experiments on the viscosity of air. Williams et al. [4] observed that the location of the maximum axial velocity is shifted towards the outer wall of a curved pipe. Later, Eustice [5] showed the existence of a secondary flow by injecting ink into water.

Due to the imbalance between inertial and centrifugal forces, a secondary motion develops in the cross section of a curved pipe. Dean [6] wrote the Navier–Stokes equations in a cylindrical reference frame, and, under the hypothesis of small curvatures and small Reynolds numbers, derived power series solutions for the stream function of the secondary motion and for the axial velocity. From his analysis a new governing parameter emerged, the Dean number De = $\mathrm{Re}\sqrt{\delta}$, which couples together inertial and centrifugal effects. Dean showed that two symmetric secondary cells develop with a characteristic velocity scale $u_{av}\sqrt{\delta}$, u_{av} being the average axial velocity and δ the dimensionless curvature defined in the following paragraphs. A thorough literature review of flow in curved pipes has been presented by Berger et al. [7].

An important engineering application of curved pipes are helical coils, which are used as heat exchangers and steam generators in power plant mainly because they are compact and easily accommodate thermal expansion; for a comparison between conventional and helically coiled heat exchangers see [8]. In particular, helical coils are also used as steam generators in some 'generation IV' nuclear reactors like IRIS [9]; this last application motivated the present study.

A schematic representation of a helical pipe with its main geometrical parameters is shown in Fig. 1. A helical coil can be geometrically described by the coil radius c, the pipe radius a, and the coil pitch $2\pi b$. The inner side will be indicated with I, the outer side with O.

The dimensionless curvature and torsion can be defined as:

$$\delta = \frac{a}{c} \tag{1}$$

$$\lambda = \frac{b}{c} \tag{2}$$

Instead of the torsion λ, the torsion parameter β is sometimes used:

$$\beta = \frac{\lambda}{\sqrt{2\delta}} \tag{3}$$

* Corresponding author. Tel.: +39 91 232 225; fax: +39 91 232 215.
E-mail address: ciofalo@din.din.unipa.it (M. Ciofalo).

1290-0729/$ – see front matter © 2009 Elsevier Masson SAS. All rights reserved.
doi:10.1016/j.ijthermalsci.2009.10.001

Nomenclature

a	inner pipe radius [m]
b	coil pitch divided by 2π [m]
c	mean coil radius [m]
c_p	specific heat [J kg^{-1} K^{-1}]
De	Dean number, Re$\sqrt{\delta}$
f	Darcy–Weisbach friction coefficient (=4 × Fanning coefficient)
k	turbulent kinetic energy [m^2 s^{-2}]
Nu	Nusselt number, $q_w 2a/\chi(T_b - T_w)$
Pr	Prandtl number, $\mu\, c_p/\chi$
q_w	wall heat flux [W m^{-2}]
Re	Reynolds number, $u_{av}\, 2a/\nu$
r	radial coordinate [m]
T	temperature [K]
u	axial velocity [m s^{-1}]
u_τ	friction velocity [m s^{-1}]
y^+	distance from the wall in wall units, $y\nu/u_\tau$

Greek symbols

δ	dimensionless curvature, a/c
λ	torsion, b/c
β	torsion parameter, $\lambda/\sqrt{2\delta}$
δ_T^+	thermal sublayer thickness in wall units
ν	kinematic viscosity [m^2 s^{-1}]
ρ	density [kg m^{-3}]
χ	thermal conductivity [W m^{-1} K^{-1}]
θ	azimuthal angle [°]
τ_w	wall shear stress [Pa]
ω	turbulence frequency [s^{-1}]

Subscripts

av	average
b	bulk
cr	critical
MIN	minimum
MAX	maximum
RAD	radial
red	reduced
s	straight pipe
SEC	section
w	wall
θ	azimuthal

Superscripts

loc	local

Helical coils reduce to curved (toroidal) pipes when $\lambda = \beta = 0$. Germano [10] presented for the first time an orthogonal reference system for helical pipes. His work prompted a number of asymptotic analyses in the laminar (low-Reynolds number) range, aimed to studying the effect of torsion on the flow. Within this strand, remarkable are the works of Chen and Jan [11], Kao [12], Xie [13], Jinsuo and Benzhao [14]. By their asymptotic approach, these authors all conclude that torsion λ has a second order effect on the flow with respect to the first order effect of curvature δ. The effect of curvature is the occurrence of two counter-rotating vortices in the cross section, while the effect of torsion is an azimuthal rotation of the centres of circulation of such cells, with a global loss of symmetry with respect to the equatorial midline I–O. In particular, Jinsuo and Benzhao [14] showed that the mass flow rate and thus the friction coefficient depend on the curvature δ, while the contribution of torsion is at most of the fourth order. Yamamoto et al. [15] performed an experimental study on pressure drop in helical coils, letting the Reynolds number Re vary from $5\cdot10^3$ to $2\cdot10^4$, the curvature δ from 0.01 to 0.1 and the torsional parameter β from 0.45 to 1.72. The authors showed that in the laminar range the influence of torsion on the friction coefficient is negligible for $\beta < 1$, i.e. $\lambda < \sqrt{2\delta}$. For example, the influence of torsion on pressure drop can be neglected for $\lambda < 0.14$ if $\delta = 0.01$, and for $\lambda < 0.45$ if $\delta = 0.1$. In the turbulent range, the authors found that the experimental data depend only on curvature for $\beta < 0.5$. In any case these values of the torsional parameter β are significantly larger than those encountered in practical engineering applications. For example, for the steam generator of the IRIS nuclear reactor [9] the torsional parameter β is of the order of $10^{-3} << 0.5$.

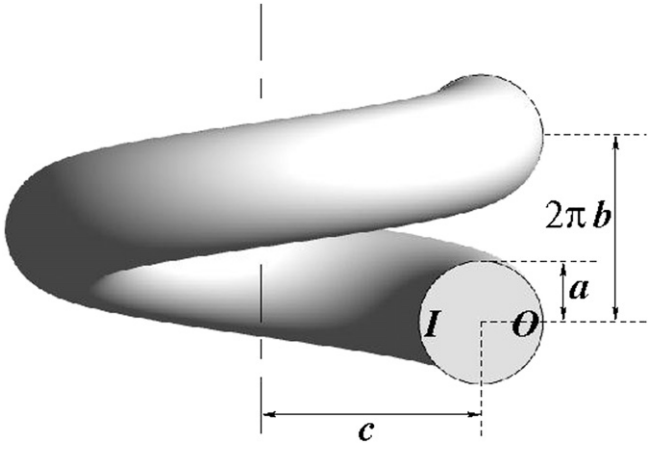

Fig. 1. Schematic representation of a helical pipe with its main geometrical parameters: a, pipe radius; c, coil radius; $2\pi b$, coil pitch. The inner (I) and outer (O) sides of the curved duct are also indicated.

The negligible effect of torsion on the global parameters is reflected in the empirical friction correlations proposed in the literature. A review of experimental results for the friction coefficient in helical coils is presented by Ali [16]; the most popular correlations are those by Ito [17]:

$$f = \frac{64}{\mathrm{Re}}\cdot\frac{21.5\cdot\mathrm{De}}{(1.56+\log_{10}\mathrm{De})^{5.73}} \quad \text{(laminar flow)} \tag{4}$$

$$f = 0.304\cdot\mathrm{Re}^{-0.25} + 0.029\sqrt{\delta} \quad \text{(turbulent flow)} \tag{5}$$

valid for $5\cdot10^{-4} \le \delta \le 0.2$. Here and in the following f is the Darcy–Weisbach friction coefficient (four times the Fanning coefficient) and the Reynolds number is defined on the basis of the inner pipe diameter as:

$$\mathrm{Re} = \frac{u_{av}2a}{\nu} \tag{6}$$

where ν is the kinematic viscosity of the fluid.

Coherently with the theoretical considerations in [14] and with the experimental evidence in [15], no practical influence of torsion is revealed by Eqs. (4) and (5), i.e. the friction coefficient depends only on the curvature δ and on the Reynolds number Re in most of the applications.

As regards the transition to turbulence, Ito [17] gives an upper bound for the applicability of the laminar flow friction correlation (4), which can be identified with a transition criterion:

$$\mathrm{Re}_{cr} = 2000(1 + 13.2\delta^{0.6}) \tag{7}$$

in the range $5\cdot10^{-4} \le \delta \le 0.2$. Eq. (7) shows that the effect of curvature is to delay transition to turbulence with respect to straight pipes. Srinivasan et al. [18] studied transition on the basis of friction coefficient measurements and proposed the following correlation for the critical Reynolds number in curved pipes:

$$\mathrm{Re}_{cr} = 2.1\cdot10^{3}(1 + 12\sqrt{\delta}) \tag{8}$$

in the range $9.7\cdot10^{-3} \le \delta \le 0.135$. Cioncolini and Santini [19] performed an experimental investigation of the friction coefficient in helical coils in a wide range of curvatures ($2.7\cdot10^{-3} \le \delta \le 0.143$) with low values of the torsion parameter ($\beta = 10^{-4}$–$2\cdot10^{-2}$), which ensures negligible torsional effects, and Reynolds numbers ranging from 10^3 to $7\cdot10^4$. The authors found a good agreement with Ito's correlations both in the laminar and in the turbulent range. For high values of the curvature ($\delta > 0.0416$), as in other relatively complex geometries [20], an abrupt transition from laminar to turbulent flow was not observed; the friction coefficient decreased monotonically with Re and transition to turbulence was indicated only by a change in slope of the f-Re curve, occurring at a Reynolds number which the authors approximated by the correlation:

$$\mathrm{Re}_{cr} = 30000\delta^{0.47} \tag{9}$$

in the range $0.0416 \le \delta \le 0.143$. For lower curvatures ($\delta < 0.0416$), Cioncolini and Santini observed that in the proximity of transition the f-Re curves exhibited a local minimum followed by an inflection point and by a local maximum; also in this range of δ they proposed transition correlations, more complex than Eq. (9) and based on identifying transition with the local minimum of f, i.e. with the first departure from the laminar behaviour.

For typical values of the curvature, Eqs. (7) through (9) yield similar values of Re_{cr}; for example, they predict $\mathrm{Re}_{cr} = 8631$, 10,069 and 10,165, respectively, for $\delta = 0.1$, and $\mathrm{Re}_{cr} = 12{,}051$, 13,370 and 14,080, respectively, for $\delta = 0.2$. Note, however, that the latter case is outside the range of validity of Eq. (8); note also that only Eqs. (7) and (8) exhibit a correct asymptotic behaviour for $\delta = 0$ (straight ducts).

Reviews of heat transfer and friction coefficient correlations in helical or curved ducts are presented by Naphon and Wongwises [21] and by Vashist et al. [22]; unfortunately, these reviews do not always specify the experimental conditions and, in some cases, do not make a clear distinction between tube-side and shell-side heat transfer correlations. Here and in the following the classical definition of the Nusselt number for the inner (tube) side will be used:

$$Nu = \frac{q_w 2a}{\chi(T_b - T_w)} \tag{10}$$

where q_w is the average wall heat flux, χ is the fluid thermal conductivity, T_b is the bulk fluid temperature and T_w is the wall temperature.

Rogers and Mayhew [23] propose the following power-law correlation based on experimental data:

$$\mathrm{Nu} = 0.023\mathrm{Re}^{0.85}\mathrm{Pr}^{0.4}\delta^{0.1} \tag{11}$$

which can be viewed as a curved-duct modification for of the well-known Dittus–Bölter correlation. It should be noticed that Eq. (11) does not exhibit the correct asymptotic behaviour for small δ, predicting $\mathrm{Nu} = 0$ for straight pipes. Many other experimental studies have been performed in the 1960s and the 1970s on the average heat transfer rate in curved and helical pipes [24,25]; only some of these investigations explored the influence of the Prandtl number on heat transfer, and very few investigated the local heat transfer rate distribution.

More recently, Xin and Ebadian [26] presented an experimental study on heat transfer in helical pipes; the authors explored two values of curvature, i.e. $\delta = 0.027$ and 0.08, Re ranging from $5\cdot10^3$ to $1.1\cdot10^5$, and used three different fluids, i.e. air ($\mathrm{Pr} = 0.7$), water ($\mathrm{Pr} = 5$), and ethylene glycol ($\mathrm{Pr} = 175$), thus covering a broad range of Prandtl numbers. The authors found that results for air and water ($0.7 < \mathrm{Pr} < 5$) can be approximated by the following correlation:

$$\mathrm{Nu} = 0.00619\mathrm{Re}^{0.92}\mathrm{Pr}^{0.4}(1 + 3.455\delta) \tag{12}$$

with an RMS deviation of 18%. Eq. (12) has the advantage of a reasonable asymptotic behaviour for straight pipes. However, a Reynolds exponent larger than 0.8 does not seem realistic, if one considers that this last value is limited to straight pipes while in more complex geometries, involving separation and reattachment, an exponent *less* than 0.8 is usually found [27].

2. Models and methods

2.1. Numerical methods

The general purpose code ANSYS CFX 11 [28] was used for all the numerical simulations presented in this paper. The code employs a coupled technique, which simultaneously solves all the transport equations in the whole domain through a false time-step algorithm. The linearized system of equations is preconditioned in order to reduce all the eigenvalues to the same order of magnitude. The multi-grid approach reduces the low frequency error, converting it to a high frequency error at the finest grid level; this results in a great acceleration of convergence. Although, with this method, a single iteration is slower than a single iteration in the classical decoupled (segregated) SIMPLE approach, the number of iterations necessary for a full convergence to a steady state is generally of the order of 10^2, against typical values of 10^3 for decoupled algorithms.

As discussed in the previous section, torsion was not considered in the present study because, for geometries of practical relevance, it has been shown that it does not significantly affect the global parameters f and Nu. Therefore, the computational domain was a short segment of a toroidal duct of circular cross section; its length was that necessary to correctly describe the curvature of the duct (a fraction of its inner radius), and was discretized by a small number of grid points.

To simulate fully developed flow and heat transfer, periodic boundary conditions were imposed at inlet–outlet, and no-slip condition for the velocity at the wall; a constant source term was added to the RHS of the axial momentum equation as the driving force per unit volume which balances pressure drop per unit length. Only one half of the section was modelled, and symmetry boundary conditions were used along the Inner–Outer symmetry plane, as shown in Fig. 2.

As thermal boundary condition, a constant wall temperature T_w was imposed. In order to apply periodic inlet–outlet boundary conditions also for the temperature field, a local energy source term was applied to compensate the wall heat flux. Taking account of the definition of the Nusselt number based on the bulk temperature T_b, this local source term must be proportional to the local axial velocity. With this treatment, the bulk temperature and the Nusselt number tend to stable values once convergence is reached. The

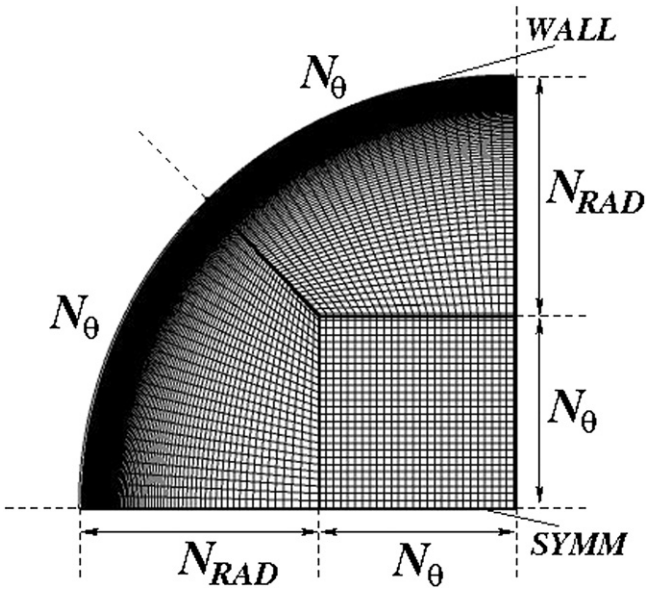

Fig. 2. Mesh (number 4) used to perform the computations. The grid is of the multi-block structured type. The total number of cells in the whole cross section would be $N_{SEC} = 4 \cdot N_\theta\,(N_\theta + 2\,N_{RAD})$, but only one half of the section is simulated.

Nusselt number thus obtained represents the asymptotic value of Nu for fully developed flow.

2.2. Turbulence modelling

Different turbulence models were used in the numerical simulations presented in this work.

The classic k–ε model [29] was adopted with a near-wall treatment (the "scalable" option in CFX-11) which practically ignores the solution within the viscous sublayer $y^+ < 11$, and imposes the universal (wall law) logarithmic solution in the first point outside of it; this approach is basically equivalent to the classic wall-function treatment with the first near-wall point outside of the viscous sublayer.

The SST (Shear Stress Transport) k–ω model by Menter [30] is formulated to solve the viscous sublayer explicitly, and requires several computational grid points inside this latter. The model applies the k–ω model close to the wall, and the k–ε model (in a k–ω formulation) in the core region, with a blending function in between. It was originally designed to provide accurate predictions of flow separation under adverse pressure gradients, but has since been applied to a large variety of turbulent flows and is now the default and most commonly used model in CFX-11 and other CFD codes.

The second order Reynolds stress–ω model (RSM–ω) was extensively used within this work. In this model, the ω-based formulation allows for an accurate near-wall treatment like in SST k–ω; diffusion terms in the Reynolds stress transport equations are treated by a simple eddy diffusivity approach, whereas great care is placed in the modelling of redistribution terms (pressure–strain rate correlations). For the exact formulation of the model and the values of the various constants, see [28].

2.3. Grid independence

A careful grid-independence study was carried out in order to provide internally coherent numerical results. The five meshes used in this study are summarized in Table 1 and are indicated as meshes 1 through 5 from the coarsest to the finest. The meshes are of the multi-block structured type, and are identified by the parameters N_{RAD} and N_θ as shown in Fig. 2. N_{SEC} represents the total number of cells in the cross section; $\Delta r_{MAX}/\Delta r_{MIN}$ is the ratio of maximum/minimum cell size in the radial direction (outer block), while the last column $y^+_{\min}$ in Table 1 is the location (in wall units ν/u_τ) of the point closest to the wall for the highest Reynolds number considered, $\mathrm{Re} = 8 \cdot 10^4$.

Table 1
Meshes used for the grid-independence study.

Mesh	N_{RAD}	N_θ	N_{SEC}	$\Delta r_{MAX}/\Delta r_{MIN}$	$y^+_{\min}$
1	38	19	7220	10	3.5
2	38	19	7220	100	0.65
3	130	27	30,996	21	0.65
4	130	27	30,996	182	0.12
5	250	43	93,396	315	0.04

Meshes 1 and 2 do not differ in the number of nodes, but only in the wall stretching parameter $\Delta r_{MAX}/\Delta r_{MIN}$ (and therefore in the wall resolution); the same holds for meshes 3 and 4. Meshes 2 and 3 have different number of nodes, but the same wall resolution. Meshes 3, 4 and 5 ensure respectively 8, 27 and 63 points within the hydrodynamic viscous sublayer $y^+ < 11$ for $\mathrm{Re} = 8 \cdot 10^4$.

For all values of the Prandtl number simulated, up to $\mathrm{Pr} = 5.6$, a correct resolution of the thermal conductive sublayer must also be ensured in order to guarantee grid-independence of the thermal results and physically consistent solutions. Experimental data reported in [31] provide a value of the thickness of the thermal viscous sublayer $\delta_T^+ = 7.55$ (in wall units) for $\mathrm{Pr} = 5.9$; on the basis of this estimate, meshes 3, 4 and 5 include 6, 22 and 51 points, respectively, within the thermal sublayer in the most critical case ($\mathrm{Pr} = 5.6$, $\mathrm{Re} = 8 \cdot 10^4$).

The results of the grid-independence study are reported in Table 2 for a typical value of the curvature, $\delta = 0.1$, and the RSM–ω model. An asymptotic tendency of the global values to converge with mesh refinement, from mesh 1 to mesh 5, can be observed. There is a significant variation from mesh 1 to mesh 2 due to the increased resolution of the viscous sublayer, and from mesh 2 to 3 due to the increased number of nodes. Both the Darcy–Weisbach friction coefficient and the Nusselt number converge, showing differences of less than 0.5% between mesh 4 and mesh 5.

On the basis of these results, mesh 4 was adopted for all the subsequent simulations conducted in the present study. Note that mesh 5 would require CPU time three times higher.

2.4. Validation by comparison with DNS results

In Table 3, computational results obtained by using the different turbulence models are compared with the results of a fully resolved direct numerical simulation (DNS). This was performed by using a grid of about $4 \cdot 10^6$ nodes with $y^+ \approx 1.2$ at the first grid point close to the wall; statistics were computed over about 20 characteristic times a/u_τ (LETOTs).

Table 2
Grid independence results for $\delta = 0.1$.

Mesh	f	Nu(Pr = 0.7)	Nu(Pr = 5.6)
1	0.025878	206.66	565.04
2	0.026032	207.13	577.96
3	0.026170	207.24	575.85
4	0.026182	211.32	572.84
5	0.026275	211.83	574.60

Table 3
Comparison with the DNS results for $\delta = 0.3$ and $\mathrm{Re} = 1.4{\cdot}10^4$.

Model	f	Nu(Pr = 0.86)
k–ε wall functions	0.033620	48.55
SST k–ω	0.053291	70.28
RSM–ω	0.055601	71.90
DNS	0.048850	65.68

The case studied is characterized by a curvature $\delta = 0.3$, a Reynolds number $\mathrm{Re} = 1.4{\cdot}10^4$, and a Prandtl number $\mathrm{Pr} = 0.86$. The values of the parameters Re and δ are the most critical for turbulence model validation, because, as it will be discussed in the next section, the largest discrepancies from experimental data are obtained for the highest curvature and the lowest Reynolds number. As a *caveat*, it must be observed that the present case may not completely satisfy the empirical criteria for fully turbulent flow discussed in the Introduction. Eqs. (7) through (9), although none of them was validated for the present curvature $\delta = 0.3$, would yield for Re_{cr} values of 14,819, 15,902 and 17,036, respectively, if stretched beyond their limits. Nevertheless, this case was chosen because DNS results were available for it and because they supported the assumption of a fully turbulent flow with a broad spectrum of velocity fluctuations.

Fig. 3 shows a comparison of the DNS average flow field in the cross section with results from the turbulence models (k–ε with near-wall treatment, SST k–ω, RSM–ω). The dimensionless temperature $(T - T_w)/(T_b - T_w)$, the dimensionless velocity u/u_{av}, and the dimensionless turbulent kinetic energy k/u_{av}^2 are represented respectively in the first, second and third column of the figure. In the DNS results, the Dean circulation is evidenced by the shape of the contours, which are deformed by the secondary jet along the wall; the Dean vortex close to the inner region is most clearly evidenced by the k contours. SST k–ω and RSM–ω yield similar velocity and temperature fields which are very close to that predicted by DNS, while the k–ε model with wall functions captures these structures only roughly. The main axial velocity contour field shows slightly better results for RSM with respect to SST in capturing flow features close to the Dean vortex.

Fig. 4 shows profiles of the dimensionless temperature as a function of the dimensionless radial coordinate r/a along the Inner–Outer direction, with $r/a = -1$ at the inner side and $r/a = 1$ at the outer side. This figure shows the different ability of the models to reproduce the main (horizontal) thermal stratification. As it was expected, k–ε completely fails in describing this stratification, while both SST and RSM results are in good agreement with DNS, with a more accurate prediction from RSM in all regions; in particular, the maximum temperature is predicted better by RSM with respect to SST.

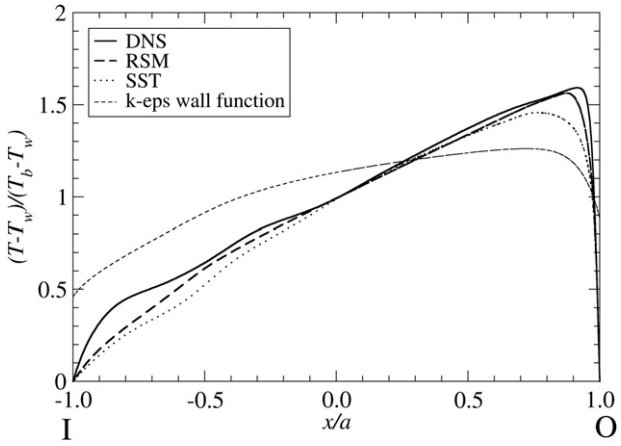

Fig. 4. Profiles of the dimensionless temperature $(T - T_w)/(T_b - T_w)$ along the Inner–Outer line for $\mathrm{Re} = 1.4{\cdot}10^4$, $\delta = 0.3$. Predictions from different turbulence models are compared with DNS average results.

Fig. 5 shows the local wall shear stress τ_w^{loc}, normalized by the mean wall shear stress τ_w, as a function of the azimuthal angle θ which increases from 0 at the inner side (I) to 180° at the outer side (O). For SST and RSM, the agreement is good for low angles ($\theta < 45$), where both models remarkably capture the Dean vortex features and the detachment point location. In the central and outer regions both models exhibit a lesser accuracy, predicting a uniform distribution of τ_w for $\theta > 90°$, whereas DNS predicts a slight monotonic increase with a maximum for $\theta = 180°$. The k–ε predictions are of far lower quality.

Fig. 6 shows the local Nusselt number Nu^{loc}, normalized by the mean Nusselt number Nu, as a function of the azimuthal angle θ. A correct overall behaviour of the plotted quantity is obtained using the SST and RSM turbulence models, which predict a growing heat

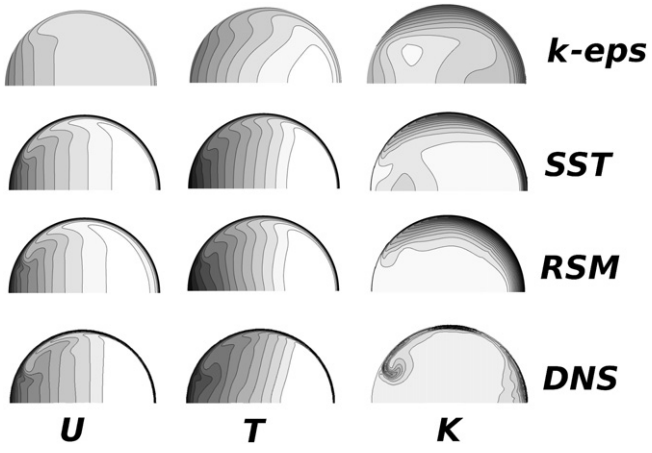

Fig. 3. Comparison of turbulence models and DNS results for $\mathrm{Re} = 1.4{\cdot}10^4$, $\delta = 0.3$. The three columns report contours of the dimensionless velocity u/u_{av} (min = 0, max = 1.2, interval = 0.1), the dimensionless temperature $(T - T_w)/(T_b - T_w)$ (min = 0, max = 1.2, interval = 0.1), and the dimensionless turbulent kinetic energy k/u_{av}^2 (min = 0, max = 0.015, interval = 0.001).

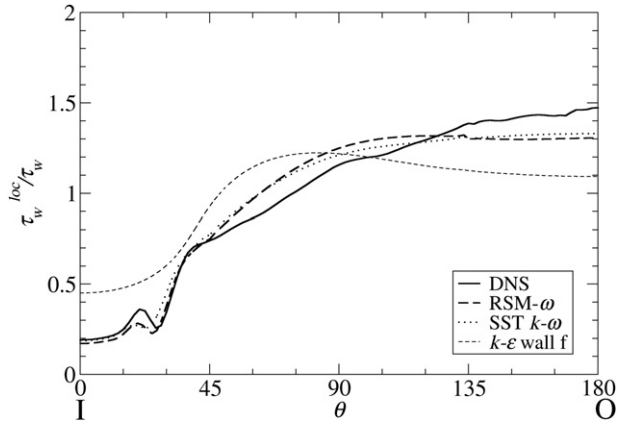

Fig. 5. Profiles of the dimensionless wall shear stress τ_w^{loc}/τ_w along the wall for $\mathrm{Re} = 1.4{\cdot}10^4$ and $\delta = 0.3$. Predictions from different turbulence models are compared with DNS average results (solid line). The azimuthal angle θ runs from 0 at the inner point to 180° at the outer point.

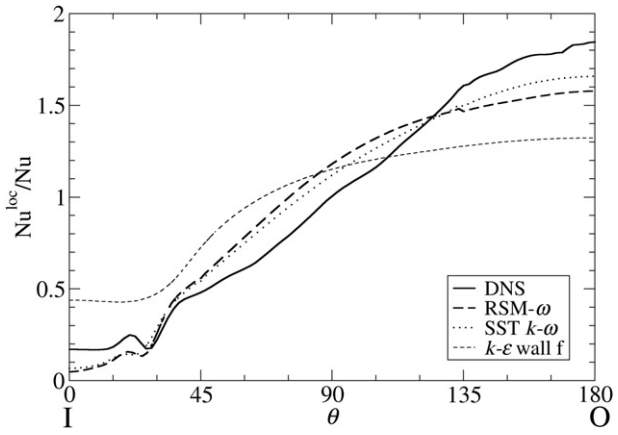

Fig. 6. Profiles of the dimensionless local Nusselt number Nu^{loc}/Nu along the wall for $Re = 1.4 \cdot 10^4$ and $\delta = 0.3$. Predictions from different turbulence models are compared with DNS average results (solid line). The azimuthal angle θ runs from 0 at the inner point to 180° at the outer point.

transfer rate going from the inner to the outer region, although an underestimate of Nu^{loc} by about 10% can be observed at the outer side ($\theta = 180°$). For low angles ($\theta < 45°$), the SST and RSM models capture the Dean vortex features and the detachment location. As in the τ_w plot, k–ε predictions are far less satisfactory and exhibit a more uniform behaviour of Nu^{loc}.

2.5. Validation by comparison with experimental pressure drop results

A comparison of results from different turbulence models with the experimental data obtained by Cioncolini and Santini [19] is discussed in this section. Turbulence models were used well into the laminar range in order to test their intrinsic ability to predict laminarization and to provide solutions in the transition region.

Fig. 7 shows a comparison of experimental and computational results for the Darcy–Weisbach friction coefficient versus Re for the geometry "COIL09" of [19], characterized by a curvature $\delta = 9.64 \cdot 10^{-3}$. The experimental data are in excellent agreement with Ito's correlations. At this relatively low value of the curvature, in the transitional region the data exhibit a "memory" of the transitional "knee" typical of the straight pipe, with a friction coefficient approximately constant from $Re = 4 \cdot 10^3$ to $Re = 10^4$.

The k–ε model with the above mentioned near-wall treatment is totally inadequate to simulate the correct behaviour of f, yielding a heavy underprediction of this quantity even in the fully turbulent region. The SST and RSM results are both in good agreement with the experimental data in the turbulent range, and are able to predict laminarization at low Re. However, they give less satisfactory results in the transitional region, predicting a smooth connection between laminar and turbulent curves; thus, they can not be fully recommended for transitional flows.

Fig. 8 shows the same comparison for a higher value of curvature, i.e. "COIL01" of [19], characterized by $\delta = 0.143$. In this case the experimental data suggest, like in complex geometries [20], a smooth transition between the laminar and the turbulent region, without any "knee"; the experimental friction coefficient curve is even smoother than in the previous case of Fig. 7 because of the more intense secondary circulation induced by the higher curvature. Also in this case the experimental data are reproduced with high accuracy by the Ito correlation, which therefore, although proposed half a century ago, can be regarded as an excellent one in its range of validity. The k–ε model underpredicts f in the whole Reynolds number range, while SST and RSM yield a good agreement with the experimental data in the turbulent range and behave better than in the lower-curvature case in Fig. 7 also in the laminar and transitional regions.

2.6. Validation by comparison with experimental heat transfer results

For heat transfer, a comparison was made with the experimental results of Xin and Ebadian [26]. Unfortunately, these authors investigate only two values of curvature, $\delta = 0.027$ and 0.08, and present most of their results in a reduced form that does not allow the original data to be retrieved. Fig. 9 shows a comparison between computational and experimental results for Nu for $\delta = 0.08$, a Prandtl number of 5 (cold water in the experiments), and Reynolds numbers in the range 10^4–$5 \cdot 10^4$. Due to the experimental method used, an additional (not declared) uncertainty of the order of ±1 is intrinsically present in the Prandtl number of the experimental study for water; therefore, it is safer to state that in the experiments Pr is in the range 4–6, i.e. 5 ± 1. Both SST and RSM

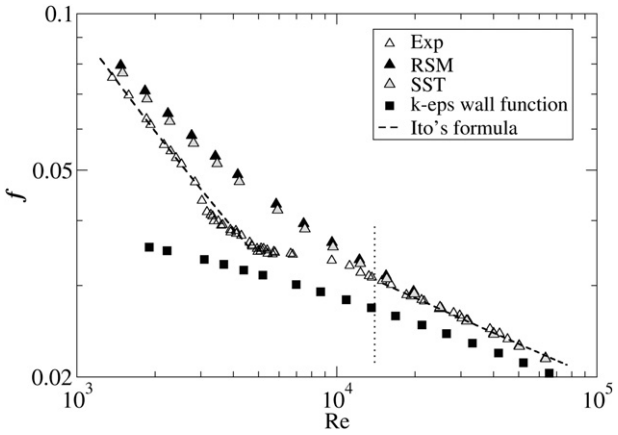

Fig. 7. Darcy–Weisbach friction coefficient as a function of the Reynolds number. Predictions from different turbulence models are compared with experimental data by Cioncolini and Santini for "COIL09" ($\delta = 9.64 \cdot 10^{-3}$). Broken lines correspond to the Ito correlations in the laminar and turbulent ranges.

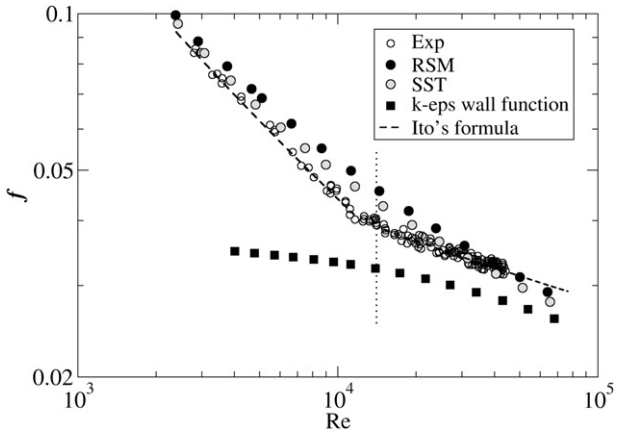

Fig. 8. Darcy–Weisbach friction coefficient as a function of the Reynolds number. Predictions from different turbulence models are compared with experimental data by Cioncolini and Santini for "COIL01" ($\delta = 0.143$). Broken lines correspond to the Ito correlations in the laminar and turbulent ranges.

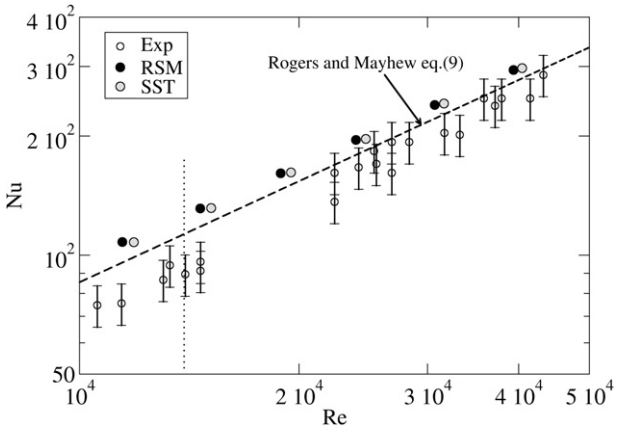

Fig. 9. Comparison of the average Nusselt number obtained by numerical simulations using the SST and RSM models with experimental data by Xin and Ebadian for $\delta = 0.08$, $Pr = 5$. Error bars for the experiments are also shown. The broken line represents the Rogers and Mayhew correlation, Eq. (9).

explicitly resolve the wall thermal and mechanical sublayers, with the first computational point at $y^+ < 0.25$ in all cases, and a substantial grid-independence of the results. In the turbulent range, both SST and RSM slightly overestimate the Nusselt number, which could partly be due to the above mentioned uncertainties on Pr. The correlation provided by Rogers and Mayhew, Eq. (11), falls in between the numerical results and the experimental data.

Fig. 10 shows a comparison of the reduced Nusselt number $Nu_{red} = NuPr^{-0.4}(1 + 3.455\delta)^{-1}$ as a function of the Reynolds number. Circles indicate the experimental data for two test sections with curvatures $\delta = 0.027$ and 0.08 and $Pr = 0.7$–5; error bars indicate the declared uncertainty on the data. Triangles show numerical results obtained using the RSM–ω turbulence model in the same range of curvature and Pr. Computational results fall within the scatter band of the experimental data; however, the experimental data themselves exhibit a relatively large dispersion once reduced by the proposed law of Eq. (12).

From the above discussions, it emerges that the SST and RSM models ensure a satisfactory and comparable accuracy in heat transfer predictions. In this work, the higher order RSM model was eventually chosen to perform the extensive parametrical study documented in the following section.

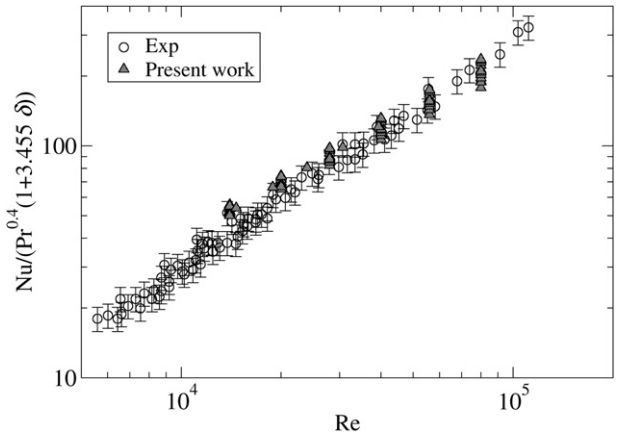

Fig. 10. Comparison of the reduced average Nusselt number $Nu\ Pr^{-0.4}\ (1 + 3.455\delta)^{-1}$ obtained by numerical simulations using the RSM model with experimental data by Xin and Ebadian for two values of the curvature ($\delta = 0.027$, 0.08) and $0.7 \leq Pr \leq 5$.

3. Parametrical study

3.1. The data set

A parametrical computational study on flow and heat transfer in curved ducts was carried out by using the second order Reynolds Stress Model (RSM–ω), in which the boundary layer was explicitly resolved and the mesh resolution guaranteed $y^+ < 0.25$ at the first grid point close to the wall even in the most critical condition. The Reynolds number Re was made to vary in the range $1.4 \cdot 10^4$–$8 \cdot 10^4$, the Prandtl number Pr in the range 0.7–5.6 and the curvature δ in the range 0–0.3. The range chosen for the Reynolds number ensures that all cases simulated fall in the full turbulent region even for the highest values of curvature and the lowest value of the Reynolds number. The range chosen for the Prandtl number covers air ($Pr = 0.7$) and water ($Pr = 1$ for water close to the saturation temperature, $Pr = 5.6$ for ambient temperature water), while the range chosen for the curvature δ includes straight pipes ($\delta = 0$) and highly curved ducts ($\delta = 0.3$), with several curvatures of practical interest in between.

A full-matrix data set was produced including six values of Re ($1.4 \cdot 10^4$, $2 \cdot 10^4$, $2.8 \cdot 10^4$, $4 \cdot 10^4$, $5.6 \cdot 10^4$, $8 \cdot 10^4$), seven values of Pr (0.7, 1, 1.4, 2, 2.8, 4, 5.6), and six values of the curvature δ ($0, 3 \cdot 10^{-3}$, 10^{-2}, $3 \cdot 10^{-2}$, 0.1, 0.3), for a total of 252 test cases. The results from all the test cases, i.e. the computed values of the Darcy friction coefficient f and of the mean Nusselt number Nu, are summarized in Table 4. Fig. 11 shows f against Re for the different δ in a doubly logarithmic scale; the friction coefficient exhibits the classic monotonic decreasing behaviour with Re, while the influence of δ is to progressively increase f. Fig. 12 shows a parity plot between computed values of the Darcy friction coefficient and those predicted by the Ito correlation (5) for turbulent flow for all the test cases in Table 4, with the exception of those at $\delta = 0.3$ which lie outside of the range of validity of Eq. (5). An excellent agreement can be observed, with an rms dispersion of a few %; the largest discrepancies are obtained for the largest f, corresponding to the lowest Reynolds number and the largest values of the curvature. Fig. 13 shows Nu against Re for the different δ in a doubly logarithmic scale and for two values of Pr, i.e. $Pr = 0.7$ and 5.6. The Reynolds number dependence of Nu follows (at least approximately) a power law, but its slope varies with Pr and δ.

3.2. The power-law dependence: a discussion

Indicating with f_s and Nu_s respectively the friction coefficient and the Nusselt number for straight ducts, and with f and Nu the corresponding quantities for a curved geometry, the ratios f/f_s and Nu/Nu_s will be used as reference quantities for discussion in this section.

If a power-law like that proposed by Xin and Ebadian, Eq. (10), held for the Nusselt number in curved ducts, and the Dittus–Bölter correlation $Nu_s = 0.023 \cdot Re^{0.8}Pr^{0.4}$ in straight ducts, the ratio Nu/Nu_s should behave as:

$$\frac{Nu}{Nu_s} = c \cdot Re^m Pr^n \cdot (1 + d \cdot \delta) \tag{13}$$

with $d = 3.455$, $m = 0.12$, $n = 0$, $c = 0.269$.

Otherwise, if the Rogers and Mayhew correlation, Eq. (11), held for curved ducts, one would obtain:

$$\frac{Nu}{Nu_s} = c \cdot Re^m Pr^n \cdot \delta^p \tag{14}$$

with $c = 1$, $m = 0.05$, $n = 0$, $p = 0.1$.

Table 4
Summary of test cases and results obtained in the present work (mesh 4, RSM–ω).

$Re \times 10^3$	$\delta \times 10^3$	$f \times 10^2$	Nu						
			Pr = 0.7	1	1.4	2	2.8	4	5.6
14	0	3.038	42.06	50.32	59.30	70.08	81.42	94.60	108.09
20	0	2.737	54.61	65.89	78.18	92.97	108.57	126.73	145.32
28	0	2.498	70.18	85.27	101.76	121.68	142.72	167.28	192.43
40	0	2.279	91.90	112.42	134.93	162.20	191.08	224.87	259.53
56	0	2.101	118.92	146.32	176.47	213.13	252.05	297.70	344.59
80	0	1.945	156.77	193.97	235.09	285.22	338.63	401.42	466.03
14	3	3.034	42.07	50.37	59.41	70.26	81.68	94.92	108.46
20	3	2.732	54.65	65.97	78.33	93.21	108.86	127.11	145.74
28	3	2.499	70.24	85.40	101.98	121.98	143.07	167.71	192.89
40	3	2.289	92.04	112.64	135.23	162.58	191.52	225.32	259.96
56	3	2.111	119.15	146.59	176.82	213.54	252.49	298.08	344.85
80	3	1.943	157.00	194.24	235.40	285.54	338.89	401.79	466.27
14	10	3.225	45.02	53.78	63.24	74.48	86.22	99.79	113.57
20	10	2.918	58.40	70.33	83.23	98.64	114.78	133.47	152.50
28	10	2.665	74.98	90.91	108.21	128.95	150.72	175.99	201.76
40	10	2.432	98.14	119.77	143.35	171.74	201.64	236.43	271.95
56	10	2.247	126.99	155.81	187.38	225.53	265.80	312.80	360.85
80	10	2.076	167.52	206.59	249.62	301.80	357.09	421.77	488.02
14	30	3.625	49.86	59.18	69.10	80.82	92.94	106.87	120.98
20	30	3.256	64.34	77.01	90.60	106.70	123.42	142.70	162.24
28	30	2.964	82.29	99.23	117.44	139.16	161.80	187.96	214.51
40	30	2.703	107.35	130.34	155.26	185.02	216.19	252.29	289.01
56	30	2.491	138.50	169.19	202.59	242.69	284.78	333.68	383.49
80	30	2.292	182.08	223.76	269.33	324.21	382.14	449.57	518.42
14	100	4.355	59.69	69.95	80.57	92.84	105.40	119.73	134.21
20	100	3.865	76.00	89.87	104.41	121.36	138.78	158.72	178.88
28	100	3.486	96.20	114.68	134.21	157.15	180.84	208.02	235.53
40	100	3.148	124.34	149.38	175.91	207.64	240.37	278.04	316.22
56	100	2.881	159.25	192.63	228.46	271.02	315.37	366.55	418.50
80	100	2.638	208.01	253.31	302.22	360.62	421.72	492.49	564.47
14	300	5.487	73.13	80.05	91.22	103.76	116.35	130.61	145.00
20	300	4.762	91.15	106.80	122.77	141.00	159.42	180.33	201.40
28	300	4.233	113.43	134.05	155.34	179.87	204.87	233.30	261.95
40	300	3.769	144.49	172.18	201.14	234.81	269.37	308.84	348.63
56	300	3.411	182.96	219.69	258.44	303.85	350.70	404.43	458.74
80	300	3.063	236.54	286.08	338.92	401.37	466.12	540.68	616.25

Apart from the exact values of the various constants, Eqs. (13) and (14) predict that power laws for the Re- and Pr-dependence, and a linear or power-law for the δ-dependence, should be observed in the computational results. However, this turns out *not* to be the case.

In particular, Fig. 14 shows a log–log diagram of f/f_s and Nu/Nu_s as functions of δ, for a fixed Reynolds number of $2 \cdot 10^4$ and all the values of the Prandtl number studied; Fig. 15 shows the same quantities in a linear–linear scale. The hydrodynamic solution, and thus the ratio f/f_s, do not depend on the Prandtl number, and Figs. 14 and 15 show that the friction coefficient ratio in a curved duct grows with the curvature δ. The Nusselt ratio Nu/Nu_s grows with the curvature regardless of the Prandtl number, but increases more rapidly for the lower values of Pr. The two graphs reveal that

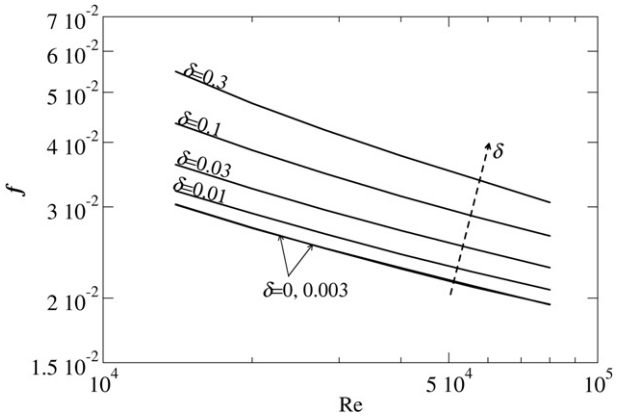

Fig. 11. Darcy–Weisbach friction coefficient as a function of the Reynolds number at different curvatures δ for the whole the computational data set. Results for $\delta = 0.003$ and $\delta = 0$ (straight pipe) are practically coincident.

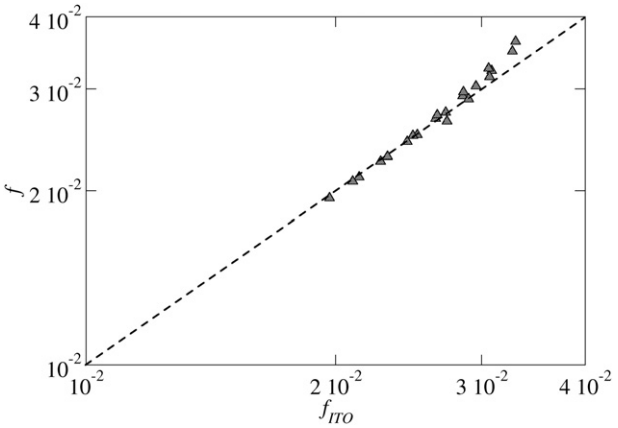

Fig. 12. Parity plot of the RSM-computed friction coefficient against that predicted by the Ito correlation.

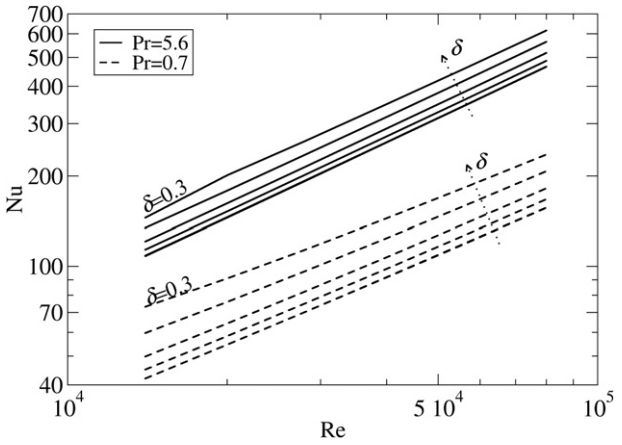

Fig. 13. RSM-computational results for the Nusselt number as a function of the Reynolds number for two values of the Prandtl number, Pr = 0.7 and 5.6. Within each family, different curves are characterized by the same values of δ as in Fig. 11.

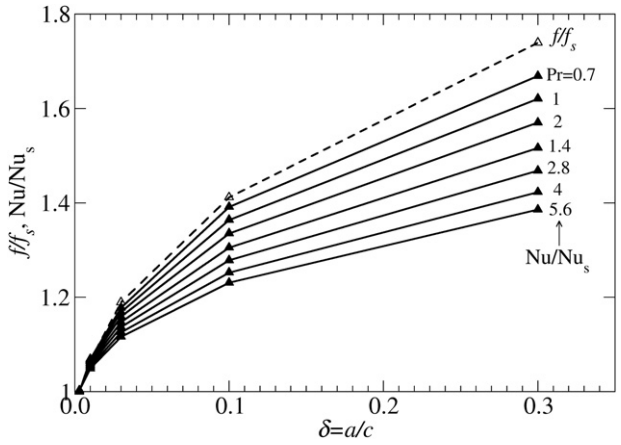

Fig. 15. Doubly linear plot of the RSM-computed relative friction coefficient f/f_s and Nusselt number Nu/Nu_s as functions of the curvature δ for $Re = 2\cdot10^4$ and different values of Pr.

neither a linear nor a power-law dependence upon the curvature δ can be found in the results for f/f_s or Nu/Nu_s. The function $(1 + d\cdot\delta)$ of Eq. (13), proposed in [26], can perhaps be applied to a small range of curvatures, but it appears as a linearization of a more complex dependence; the power-law δ^p dependence of Eq. (14) is also not respected and, moreover, does not provide the correct asymptotic behaviour of Nu/Nu_s for $\delta\to0$.

Fig. 16 shows a log–log diagram of f/f_s and Nu/Nu_s as functions of Pr, for a fixed Reynolds number of $2\cdot10^4$ and different values of the curvature. The hydrodynamic solution and thus the ratio f/f_s do not depend on the Prandtl number, and therefore the corresponding curves are horizontal lines for any value of δ. In the range examined, the Nusselt number ratio remains always smaller than the friction coefficient ratio. An inverse power-law dependence on Pr can be observed for the Nusselt ratio at all values of δ, but the power exponent increases in absolute value with the curvature instead of being a constant: therefore, the dependence of Nu/Nu_s upon Pr predicted by Eqs. (13) and (14) is not confirmed, while a $Pr^{-n\delta}$ law would be more coherent with the results. A similar behaviour is observed for higher Reynolds numbers. For a given value of the curvature, the slope of the Nu/Nu_s lines decreases in absolute value with the Reynolds number, as shown in Fig. 17 where Nu/Nu_s is plotted against Pr for various Re. A hypothetical power-law dependence on Pr should be of the form $Pr^{-n\delta g(Re)}$, $g(Re)$ being a decreasing positive function of the Reynolds number.

Fig. 18 shows a log–log diagram of f/f_s and Nu/Nu_s as functions of Re, for Pr = 1 and 4 and different values of the curvature δ. The Reynolds number dependence appears to be weak, especially at moderate values of the curvature δ, i.e. $\delta \le 0.03$. Therefore, also in this case a hypothetical Reynolds number exponent for Nu/Nu_s should be negative, which is consistent with the above mentioned fact that in complex flows with recirculation the Nu–Re power-law exponent is systematically lower than the value 0.8 typical of simple geometries. Moreover, such exponent would depend on δ and Pr, and only a $Re^{-m\delta g(Pr)}$ law would be approximately consistent with the numerical results.

The above analysis shows that the simple, empirically based, power-law dependences proposed in the literature can not account for the complexity of the real functional dependences, and a different approach is necessary for a correct regression of the data set.

3.3. Heat transfer-momentum analogy

Churchill [32] presents a critical review of the classical algebraic analogies between heat, mass and momentum transfer, and derives

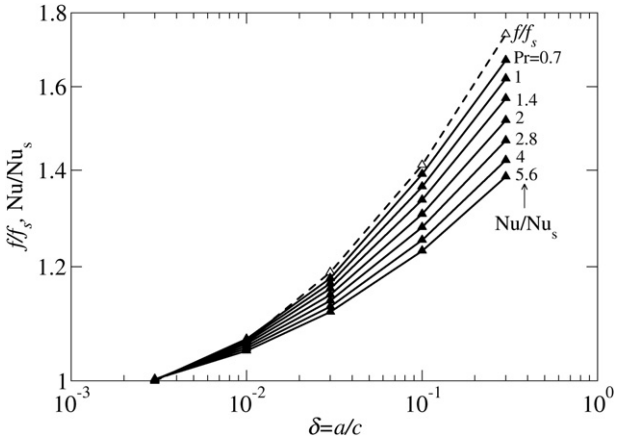

Fig. 14. Doubly logarithmic plot of the RSM-computed relative friction coefficient f/f_s and Nusselt number Nu/Nu_s as functions of the curvature δ for $Re = 2\cdot10^4$ and different values of Pr.

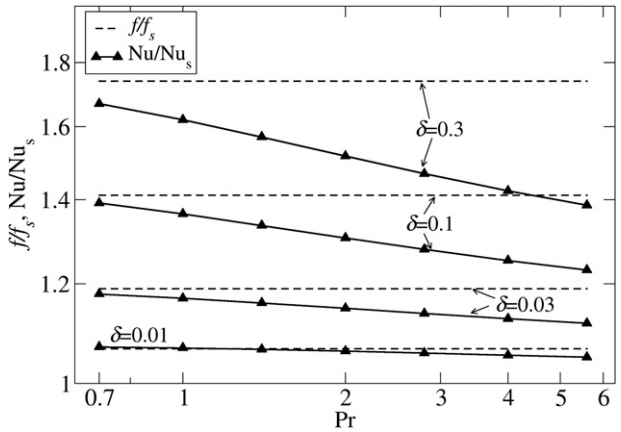

Fig. 16. Doubly logarithmic plot of the RSM-computed relative friction coefficient f/f_s and Nusselt number Nu/Nu_s as functions of Pr for $Re = 2\cdot10^4$ and different values of δ.

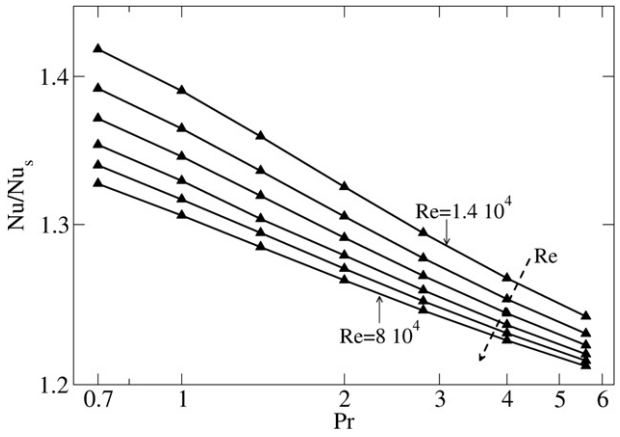

Fig. 17. Doubly logarithmic plot of the RSM-computed relative Nusselt number Nu/Nu_s as a function of Pr for $\delta = 0.1$ and Re ranging from $1.4 \cdot 10^4$ to $8 \cdot 10^4$.

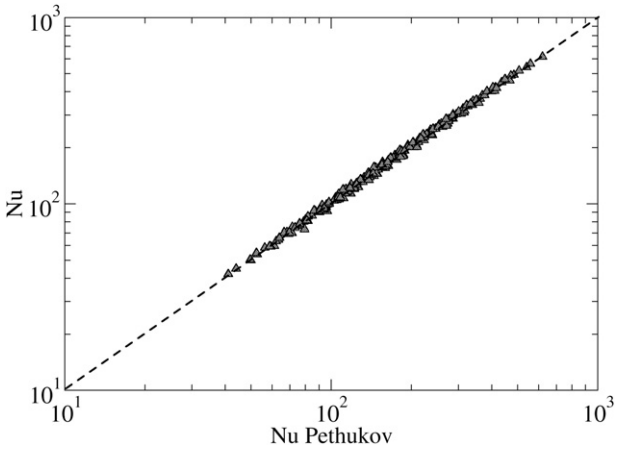

Fig. 19. Parity plot of the mean Nusselt number computed by CFD using the RSM–ω turbulence model against that predicted by the Pethukov analogy using computed values of f.

an exact integral formulation of the momentum-heat transfer analogy for circular ducts. The author shows that, surprisingly, very popular power-law formulas like the Colburn analogy:

$$\mathrm{Nu} = \mathrm{Pr}^{1/3}\mathrm{Re}\cdot(f/8) \tag{15}$$

are not physically founded or theoretically based, but are only used for traditional reasons or because they are easy to manipulate. For example, Churchill shows that the correct asymptotic behaviour of the Nusselt number for $\mathrm{Pr} \to \infty$ should be $\mathrm{Re}(f/8)^{1/2}$, and not $\mathrm{Re}(f/8)$ as prescribed by the Reynolds–Colburn analogy.

Pethukov [33] correlated experimental values of the Nusselt number for turbulent straight pipe flow and for $0.5 \leq \mathrm{Pr} \leq 2000$ by the expression:

$$\mathrm{Nu} = \frac{\mathrm{PrRe}(f/8)}{1.07 + 12.7\sqrt{f/8}(\mathrm{Pr}^{2/3} - 1)} \tag{16}$$

Eq. (16) is based on the same general integral analogy used later by Churchill [32], with an eddy diffusivity model for the Reynolds stresses, and therefore it rests on a more sound theoretical ground than the simple Dittus–Bölter power-law. In fact, for straight pipes Eq. (16) provides a greater accuracy, with a deviation of only a few percent with respect to experimental data.

Therefore, it is worth checking whether Pethukov's analogy, Eq. (16), can successfully be applied also to curved pipes, i.e. can lead to a reduction of the dispersion with respect to power-law correlations. In the literature on curved ducts, only Seban and McLaughlin [24] introduce the friction coefficient as a modelling parameter for the Nusselt number, but maintain a power-law dependence on the Prandtl number.

In Fig. 19, a parity plot is presented of the CFD-computed Nusselt number against the Pethukov predictive formula (16), in which for the Darcy friction coefficient the values computed by CFD for curved geometries, Table 4, were used. The numerical data collapse very well with an RMS dispersion of only 1–2%. As Fig. 12 suggests, very similar results would be obtained by correlating computed values of Nu with those predicted by substituting the values of f given by Ito's correlation (5) into the Pethukov analogy (16). Fig. 20 shows such a parity plot of Nu against the Pethukov formula (16). This shows that the combination of Eqs. (5) and (16) predicts Nu in curved ducts with the same accuracy of the present RSM–ω simulations and is far superior to previously suggested correlations.

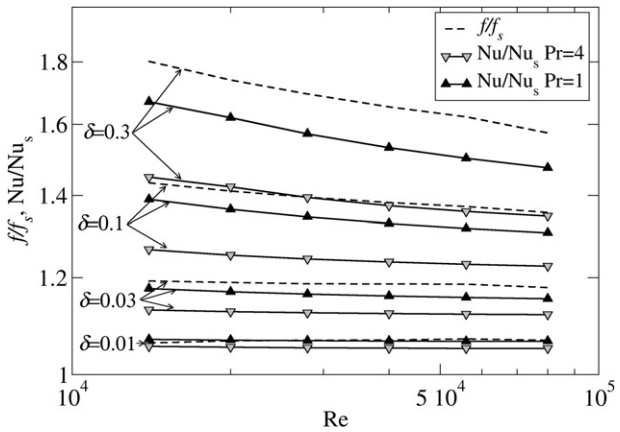

Fig. 18. Doubly logarithmic plot of the RSM-computed relative friction coefficient f/f_s and Nusselt number Nu/Nu_s as functions of Re for $\mathrm{Pr} = 1$ and 4 and different values of δ.

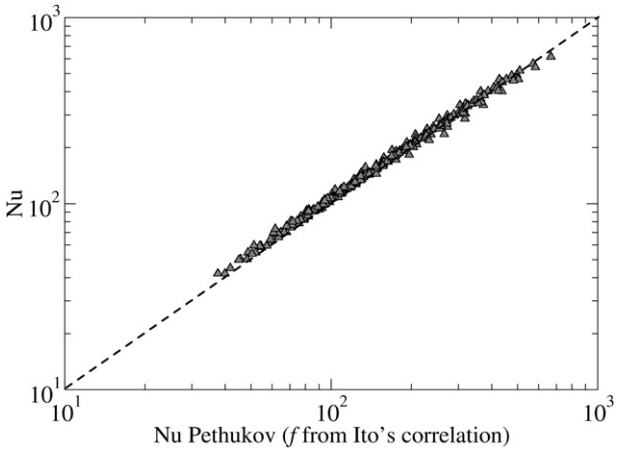

Fig. 20. Parity plot of the mean Nusselt number computed by CFD using the RSM–ω turbulence model against that predicted by the Pethukov analogy using the values of f given by the Ito correlation.

4. Conclusions

To the best of the authors' knowledge, this is the first systematic attempt to assess the applicability of alternative turbulence models to the prediction of pressure drop and heat transfer in coiled tubes in a broad range of geometrical and physical conditions.

The comparison of alternative turbulence models showed that the SST k–ω eddy viscosity/eddy diffusivity model and the second order Reynolds Stress–ω model give comparable results for the friction coefficient f and the Nusselt number Nu, the latter being slightly better in predicting details of velocity and temperature profiles when compared with direct numerical simulations. Moreover, both models are able to predict laminarization and thus are applicable with only a moderate error also to Reynolds numbers below the transition to fully turbulent flow (i.e, in the laminar and transitional range). The standard k–ε model, with a near-wall treatment equivalent to using classic wall functions, yields a severe underprediction of both f and Nu. This shortcoming is not surprising since, in the present geometry, the turbulence structure in the near-wall layer departs significantly from the conditions (flat plate, equilibrium boundary layer) for which wall functions are tuned; suffice it to remember that an impingement region exists in the outer wall of the coil and a detachment region in the inner wall.

The application of the RSM–ω model in the fully turbulent regime ($\mathrm{Re} > 1.4 \cdot 10^4$) for different values of the curvature δ yields pressure drop results in excellent agreement with experimental data [19] and with the correlation proposed by Ito [17]. Heat transfer results obtained for different Prandtl numbers in the range 0.7–5.6 are in good agreement with published experimental results [26] but are poorly described by simple power-law correlations. Instead, the use of a properly formulated momentum-heat transfer analogy, notably in the form known as the Pethukov correlation [33], yields an excellent reduction of all heat transfer data, using either the CFD-computed friction coefficient or that predicted by the Ito correlation [17]. This is, in the authors' opinion, the most significant conclusion of the present study.

References

[1] M.J. Boussinesq, Mémoire sur l'influence des frottements dans les mouvements régulier des fluides. J. de Mathématiques Pures Appliquées 2me Série 13 (1868) 377–424.
[2] J. Thomson, On the origin of windings of rivers in alluvial plains, with remarks on the flow of water round bends in pipes. Proc. R. Soc. Lond. Ser. A 25 (1876) 5–8.
[3] J.H. Grindley, A.H. Gibson, On the frictional resistance to the flow of air through a pipe. Proc. R. Soc. Lond. Ser. A 80 (1908) 114–139.
[4] G.S. Williams, C.W. Hubbell, G.H. Fenkell, On the effect of curvature upon the flow of water in pipes. Trans. ASCE 47 (1902) 1–196.
[5] J. Eustice, Experiment of streamline motion in curved pipes. Proc. R. Soc. Lond. Ser. 85 (1911) 119–131.
[6] W.R. Dean, Note on the motion of the fluid in a curved pipe. Phil. Mag. 4 (1927) 208–223.
[7] S.A. Berger, L. Talbot, L.S. Yao, Flow in curved pipes. Ann. Rev. Fluid Mech. 15 (1983) 461–512.
[8] G.S.V. Prabhanjan, G. Raghavan, T.J. Rennie, Comparison of heat transfer rates between a straight tube heat exchanger and a helically coiled heat exchanger. Int. Comm. Heat Mass Transf. 29 (2002) 185–191.
[9] M.D. Carelli, L.E. Conway, L. Oriani, B. Petrović, C.V. Lombardi, M.E. Ricotti, A.C.O. Barroso, J.M. Collado, L. Cinotti, N.E. Todreas, D. Grgić, M.M. Moraes, R.D. Boroughs, H. Ninokata, D.T. Ingersoll, F. Oriolo, The design and safety features of the IRIS reactor. Nucl. Eng. Des. 230 (2004) 151–167.
[10] M. Germano, On the effect of torsion in a helical pipe flow. J. Fluid Mech. 125 (1982) 1–8.
[11] W.H. Chen, R. Jan, The characteristics of laminar flow in helical circular pipe. J. Fluid Mech. 244 (1992) 241–256.
[12] H.C. Kao, Torsion effect on fully developed flow in a helical pipe. J. Fluid Mech. 184 (1987) 335–356.
[13] G.D. Xie, Torsion effect on secondary flow in helical pipes. Int. J. Heat Fluid Flow 11 (1990) 114–119.
[14] Z. Jinsuo, Z. Benzhao, Fluid flow in a helical pipe. Acta Mech. Sin. 15 (1999) 299–312.
[15] K. Yamamoto, T. Akita, H. Ikeuki, Y. Kita, Experimental study of the flow in a helical circular tube. Fluid Dyn. Res. 16 (1995) 237–249.
[16] S. Ali, Pressure drop correlations for flow through regular helical coil tubes. Fluid Dyn. Res. 28 (2001) 295–310.
[17] H. Ito, Friction factors for turbulent flow in curved pipes. J. Basic Eng. 81 (1959) 123–134.
[18] S. Srinivasan, S. Nadapurkar, F.A. Holland, Friction factors for coils. Trans. Inst. Chem. Eng. 48 (1970) T156–T161.
[19] A. Cioncolini, L. Santini, An experimental investigation regarding the laminar to turbulent flow transition in helically coiled pipes. Exp. Thermal Fluid Sci. 30 (2006) 367–380.
[20] J.A. Stasiek, M.W. Collins, M. Ciofalo, P.E. Chew, Investigation of flow and heat transfer in corrugated passages – I. Experimental results. Int. J. Heat Mass Transf. 39 (1996) 149–164.
[21] P. Naphon, S. Wongwises, A review of flow and heat transfer characteristics in curved tubes. Renewable Sustain. Energy Rev. 10 (2006) 463–490.
[22] S. Vashisth, V. Kumar, D.P.K. Nigam, A review on the potential application of curved geometries in process industry. Ind. Eng. Chem. Res. 47 (2008) 3291–3337.
[23] G.F.C. Rogers, Y.R. Mayhew, Heat transfer and pressure loss in helically coiled tubes with turbulent flow. Int. J. Heat Mass Transf. 7 (1964) 1207–1216.
[24] R.A. Seban, E.F. McLaughlin, Heat transfer in tube coils with laminar and turbulent flow. Int. J. Heat Mass Transf. 6 (1963) 387.
[25] Y. Mori, W. Nakayama, Study of forced convective heat transfer in curved pipes. Int. J. Heat Mass Transf. 11 (1967) 681.
[26] R.C. Xin, M.A. Ebadian, The effects of Prandtl numbers on local and average convective heat transfer characteristics in helical pipes. J. Heat Transf. 119 (1997) 467–473.
[27] M. Ciofalo, M.W. Collins, k–ε predictions of heat transfer in turbulent recirculating flows using an improved wall treatment. Num Heat Transf. 15 (1989) 21–47.
[28] ANSYS CFX Release 11 User Manual.
[29] B.E. Launder, D.B. Spalding, The numerical computation of turbulent flows. Comput. Methods Appl. Mech. Eng. 3 (1974) 269–289.
[30] F.R. Menter, Two-equation eddy-viscosity turbulence models for engineering applications. AIAA J. 32 (1994) 269–289.
[31] W.M. Kays, M.E. Crawford, Convective Heat and Mass Transfer. McGraw-Hill, New York, 1993.
[32] S.W. Churchill, Critique of the classical algebraic analogies between heat, mass and momentum transfer. Ind. Eng. Chem. Res. 36 (1997) 3866–3878.
[33] B.S. Pethukov, Heat transfer and friction in turbulent pipe flow with variable physical properties. Adv. Heat Transf. 6 (1970) 1–69.